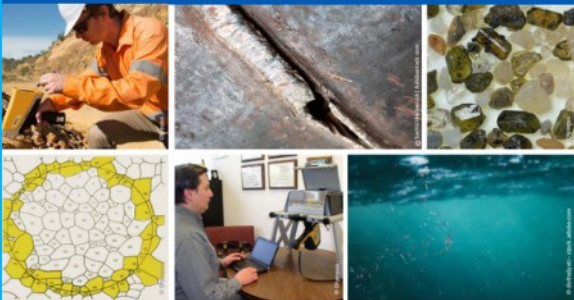# 2nd Advanced Optical Metrology Compendium

## Advanced Optical Metrology

Geoscience | Corrosion | Particles | Additive
Manufacturing: Metallurgy, Cut Analysis & Porosity

EVIDENT
OLYMPUS

WILEY

**The latest eBook from Advanced Optical Metrology. Download for free.**

This compendium includes a collection of optical metrology papers, a repository of teaching materials, and instructions on how to publish scientific achievements.

With the aim of improving communication between fundamental research and industrial applications in the field of optical metrology we have collected and organized existing information and made it more accessible and useful for researchers and practitioners.

EVIDENT
OLYMPUS

WILEY

# 3D Printed Tubular Scaffolds with Massively Tailorable Mechanical Behavior

*Edmund Pickering,\* Naomi C. Paxton, Arixin Bo, Bridget O'Connell, Mitchell King, and Maria A Woodruff*

Melt electrowriting (MEW) is a promising additive manufacturing technique for tissue scaffold biofabrication. Successful application of MEW scaffolds requires strictly controlled mechanical behavior. This requires scaffold geometry be optimized to match native tissue properties while simultaneously supporting cell attachment and proliferation. The objective of this work is to investigate how geometric properties can be exploited to massively tailor the mechanical behavior of tubular crosshatch scaffolds. An experimentally validated finite element (FE) model is developed and 441 scaffold geometries are investigated under tension, compression, bending, and radial loading. A range of pore areas (4–150 mm$^2$) and pore angles (11°–134°) are investigated. It is found that scaffold mechanical behavior is massively tunable through the control of these simple geometric parameters. Across the ranges investigated, scaffold stiffness varies by a factor of 294× for tension, 204× for compression, 231× for bending, and 124× for radial loading. Further, it is discussed how these geometric parameters can be simultaneously tuned for different biomimetic material applications. This work provides critical insights into scaffold design to achieve biomimetic mechanical behavior and provides an important tool in the development of biomimetic tissue engineered constructs.

## 1. Introduction

Melt electrowriting (MEW) is a novel additive manufacturing (3D printing) technology widely explored in biofabrication and tissue engineering for manufacturing of microfiber scaffolds.[1,2] Using an electrohydrodynamic jet of molten material, a continuous microfiber is deposited onto a collector, layer by layer, in a precisely controlled pattern. Often, low melting temperature, semicrystalline thermoplastics, like poly-caprolactone (PCL), are preferred due to their low melt temperature, viscosity conducive to extrusion using low-cost air pressure regulation or syringe pumps, rapid solidification, and biocompatibility.[3–5] MEW benefits from being an open-source technology, enabling versatility in machine design. This enables optimization for different collector surfaces (e.g., flat or cylindrical), material extrusion modalities (e.g., syringe pumps or air pressure driven), heating configurations, and high voltage configurations.[6,7] Together, this enables the fabrication of MEW scaffolds with complex morphologies and with precisely controlled 3D fiber networks. These 3D fiber networks have been explored for their highly tunable mechanical properties and subsequent influence on cell attachment, proliferation, and tissue regeneration for a range of applications.[1,8,9]

The ability to fabricate tubular MEW scaffolds using a rotating mandrel is of growing interest and has been demonstrated in various works,[7–22] with proposed tissue engineering applications including vascular,[9,14,17,22] bone,[10,17] kidney,[12] and heart valve.[13] Tubular scaffolds with aligned fiber meshes[16,17] and crosshatch (or "diamond") patterns[18] are most often reported. The close relationship between MEW fiber patterning and scaffold mechanics is of significant interest in many studies where the mechanical behavior can influence the biomechanical suitability for the selected tissue engineering application, for example, in replicating the mechanics of tissues like heart valves[21,23] or kidney tubules.[12] Further, scaffold geometry can influence the biological response of seeded cells, including attachment,[24] alignment,[25] and tissue maturation.[26,27] While emerging research is expanding the range of patterns printable on rotating mandrels to include stent-like geometries,[9] multilayered tubular structures,[19,27] as well as expandable auxetic structures,[22,28] crosshatch patterns remain the most widely studied in the MEW literature, primarily due to the low burden in print path programming[29] and infancy of MEW hardware to enable more complex patterning.

The capacity to vary tubular scaffold mechanical behavior through geometric variables has been demonstrated;[13,22]

E. Pickering, N. C. Paxton, A. Bo, B. O'Connell, M. King, M. A. Woodruff
School of Mechanical, Medical and Process Engineering
Queensland University of Technology (QUT)
Brisbane 4000, Australia
E-mail: ei.pickering@qut.edu.au

E. Pickering, N. C. Paxton, M. A. Woodruff
Centre for Biomedical Technologies
Queensland University of Technology (QUT)
Brisbane 4000, Australia

A. Bo
INM – Leibniz Institute for New Materials
66123 Saarbrücken, Germany

The ORCID identification number(s) for the author(s) of this article can be found under https://doi.org/10.1002/adem.202200479.

however, little effort has been expended on the mechanical tunability of such scaffolds. To overcome this challenge, this study aims to develop an automated model to predict the mechanical properties of crosshatch MEW. A robust finite element (FE) model, based upon beam elements, was developed to model the mechanical deformation of scaffolds under tension, compression, bending, and radial loading, corresponding to the four most widely studied mechanical loading conditions experienced by tissue engineered constructs in development for musculoskeletal, cardiovascular, and renal applications.[12,13,19,30] As beam elements are significantly less computationally expensive than the more common brick elements, this enables rapid modeling of scaffold geometries. Using this, we undertook the first comprehensive study of crosshatch tubular scaffold geometric parameters and their effect on scaffold mechanics. This consolidates findings from experimental characterization of different fiber laydown angles,[18] pore sizes and fiber spacing,[12] into a continuous model to predict scaffold mechanical behavior and reverse engineer scaffold design parameters for ideal biomimetic performance. Further, this study reveals the massive tailorability of this scaffold design.

## 2. Results

### 2.1. Scaffold Geometry and Nomenclature

Nomenclature of the tubular scaffolds is detailed in **Figure 1**a. The geometry of each scaffold is defined by its length ($l$), radius ($r$), number of circumferential junctions ($N_c$), number of longitudinal junctions ($N_l$), pore area $\left(A_{pore} = \frac{1}{2} \frac{2\pi r}{N_c} \frac{L}{N_l}\right)$, and pore angle $\left(\beta = \pi - 2\mathrm{atan}\left(\frac{L}{N_l} \frac{N_c}{2\pi r}\right)\right)$. Figure 1b–f indicates the loading conditions investigated in this work.

The following terms are further defined. A fiber refers to a single strand of material produced using MEW. A thread consists of multiple MEW fibers stacked on top of each other, resulting in multiple bonded fibers (see **Figure 2**a). A junction refers to the intersection of two threads. A strut refers to the segment of a thread between two junctions.
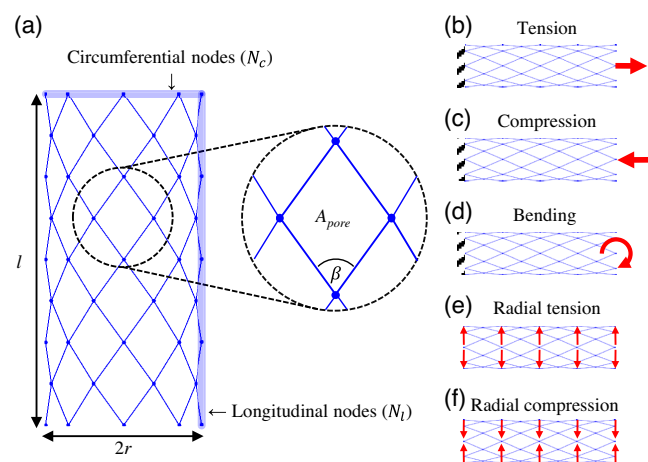
### 2.2. Mechanical Testing of Single MEW Threads

To determine the mechanical properties of MEW polycaprolactone (PCL) threads, 12 threads were fabricated, and subsequently tested under uniaxial tension. Each thread is 120 mm in length and consists of ten fibers.

Under scanning electron microscope (SEM) observation individual fibers appeared to be neatly stacked and well bonded, with no apparent defects (Figure 2a). At the junction, some fiber separation is observed; this is a common phenomenon in MEW scaffolds.[31] Each fiber had a roughly circular cross section with a mean diameter of 21.6 μm, resulting in a total thread height of 216 μm. Idealizing the thread cross section as a rectangle, the idealized thread area was 4666 μm² (see Section S1, Supporting Information).

An indicative stress–strain curve of a single thread is shown in Figure 2b. This curve is typical of PCL fibers reported in the literature,[32–34] although some variance can be expected due to variance in molecular length and printing conditions. In general, the threads undergo linear-elastic deformation with an elastic modulus of $448 \pm 33$ MPa up to a yield stress of $22.0 \pm 1.7$ MPa at $7.77 \pm 1.27\%$ strain, followed by the stress plateaus at $17.7 \pm 1.6$ MPa, before increasing to an ultimate strength of $30.1 \pm 3.5$ MPa and failure at $738 \pm 91\%$ strain (results presented are mean $\pm$ standard deviation).

### 2.3. Experimental Validation of FE Scaffold Model

A FE model was developed to predict the behavior of MEW tubular crosshatch scaffolds. To validate the model, crosshatch tubular scaffolds were fabricated with pore angles of 21.8°, 53.8°, and 95.4° (diameter of 16 mm, length of 40 mm, target pore area of 0.5 mm², ten fibers per thread). Under SEM inspection, the fabricated scaffolds were found to be of high quality, with neatly stacked fibers.

The fabricated scaffolds were tested under uniaxial tension, and likewise simulated via the FE model. The FE model accurately predicted the tensile behavior and deformed shape of the MEW scaffolds. **Figure 3** shows the validation study, comparing FE predictions against experimental results. Depending on the scaffold nature, the force–displacement curve under tensile loading can be separated into two or three distinct sections (see Figure 3a). The 53.8° and 95.4° scaffolds first exhibit a low-stiffness toe region, followed by a transition (heel) to high-stiffness linear region, before eventual plastic deformation. The 21.8° scaffold did not exhibit a toe region, rather only exhibits high-stiffness linear-elastic deformation and plastic deformation.

Comparison of the force–displacement curves for the experimental and FE tests (Figure 3a) demonstrates the validity of the FE model in predicting the behavior of MEW scaffolds. Specifically, under tensile loading, the FE model predicted the elastic deformation of the scaffolds (i.e., toe region, transition (heel), and linear region). As a linear-elastic material model was employed, the limit of the FE model's validity is at the transition from elastic to plastic deformation in the experimental data. This is observed by a distinct deviation between the two data sets. Within the valid region, the maximum deviation is 0.33, 0.42, and 0.24 N for the 21.8°, 53.8°, and 95.4° cases, respectively (see Section S2, Supporting Information).
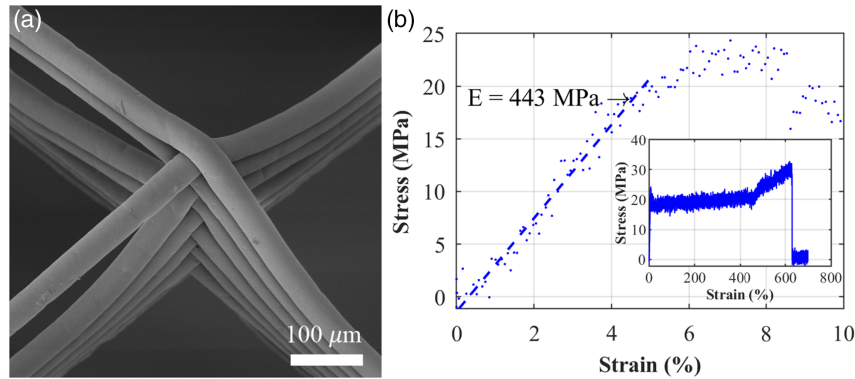


**Figure 1.** a) Geometric variables and nomenclature of the MEW scaffolds. b–f) Loading types investigated in this study.

**ADVANCED
SCIENCE NEWS**

www.advancedsciencenews.com

**ADVANCED
ENGINEERING
MATERIALS**

www.aem-journal.com

**Figure 2.** a) SEM micrograph of scaffold junction showing intersecting threads. b) Example tensile test of a single thread with an elastic modulus of 436 MPa.
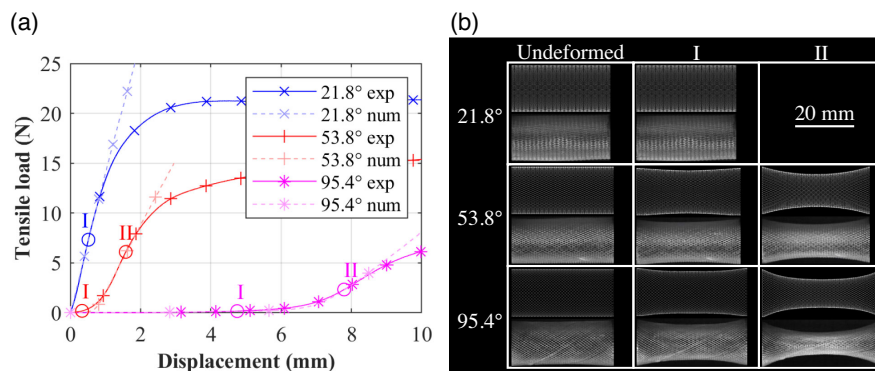


**Figure 3.** Experimental validation showing, a) load–displacement data from the experimental and numerical studies, and b) comparison of the experimental and numerical deformed scaffolds. For each case, the upper image is numerical and the lower image is experimental. Points I and II represent approximate midpoints on the toe and linear regions.

In addition, the FE model also accurately predicted the deformed shapes of the scaffolds. Figure 3b compares the deformed shape from the experimental and FE tests for points (I) and (II) (as shown in Figure 3a). In this, the deformed shape predicted by the FE model closely matches that observed experimentally, during the elastic deformation stages.

These results demonstrate the validity of the FE model in predicting elastic deformation behaviors of the studied scaffolds under tensile loading. It is important to note that the scaffolds tensile deformation behavior is complex, encompassing large deformation, shape change, and nonaxial fiber motion. The deformation mechanism presented here is the deformation of individual struts. By extension, the model is thus considered valid under compression, bending, and radial loading, which embody these same deformation mechanisms, and are commonly considered loading regimes for tubular scaffolds and are thus of interest in this study. This is in line with other studies of similar constructs, which have validated under one loading condition and then extended to other conditions.[35,36]

## 2.4. FE Predictions of Deformation Behavior

Using the experimentally validated FE model, the mechanical behavior of crosshatch tubular scaffolds under tension,

compression, bending, and radial loading was investigated. First, the impact of pore angle was explored (maintaining constant pore area). Second, the impact of varying pore angle and area was investigated. To better replicate the geometry of vascular stents, scaffolds simulated in this section were 20 mm in length and 3 mm in diameter.[37]

### 2.4.1. Tensile

The FE model revealed the complex tensile behavior of crosshatch tubular scaffolds (see **Figure 4**). When considering the impact of pore angle (with constant pore area), the force–deformation behavior varied dramatically across the range of pore angles investigated (see Figure 4a–c).

For scaffolds with a large pore angle, a clear bilinear behavior was observed, with an initial low-stiffness toe region, followed by transition to a high-stiffness linear region (matching experimental observation). As the pore angle reduced, the toe region became less prominent, and for scaffolds with a pore angle below approximately 20°, the toe region was not observed.

Simultaneously, the tensile stiffness varies dramatically with respect to pore angle (see Figure 4b), which can be used to effectively tune scaffold stiffness. Over the pore angles investigated here, the initial stiffness varied by a factor of 294× (from 2.91
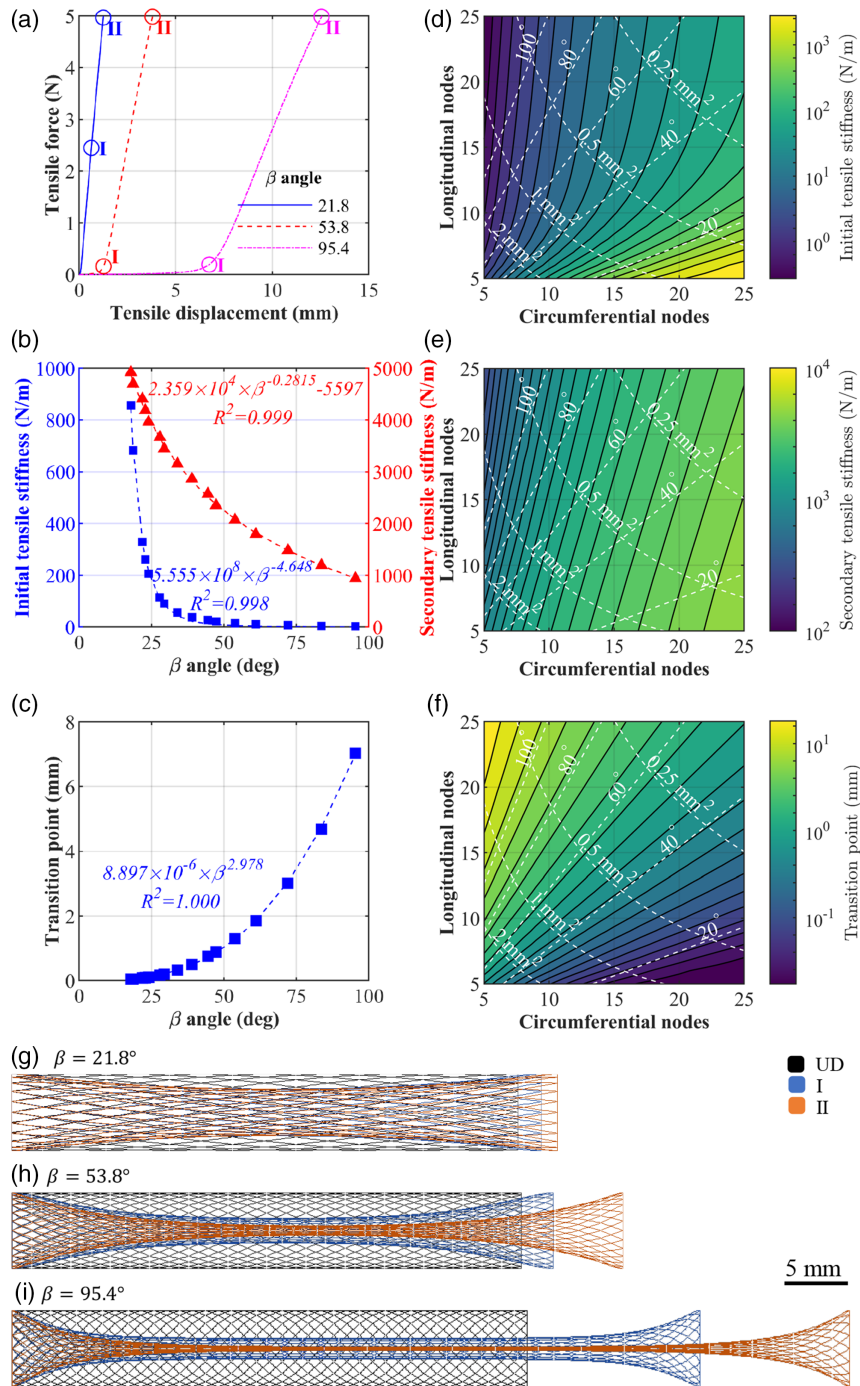
**ADVANCED
SCIENCE NEWS**

www.advancedsciencenews.com

**ADVANCED
ENGINEERING
MATERIALS**

www.aem-journal.com

**Figure 4.** Tensile behavior of scaffolds predicted by FE model. a) Force–displacement curve of the indicative scaffolds, showing typical behavior. b) Initial and secondary stiffness of the scaffolds as a function of pore angle. c) Transition point from initial stiffness to secondary stiffness as a function of varying pore angle. d–f) Color maps of (d) initial stiffness, (e) secondary stiffness, and (f) transition point as a function of pore angle and pore area (or circumferential and longitudinal nodes). g–i) Deformation behavior of the indicative scaffolds from (a) showing the scaffold morphology in their undeformed (UD) state, partially deformed state (I) and maximally deformed state (II). For the 53.8° and 94.5° scaffolds, state (I) is at the transition point. For the 21.8° scaffold, state (I) is at half the maximum deformation.

to 857 N m$^{-1}$). Likewise, the secondary stiffness varied by a factor of 5.24× (from 939 to 4920 N m$^{-1}$).

The mechanism for this massive variance can be found in the structure and deformed morphologies of the scaffolds (shown in

Figure 4g–i). For low pore angle, the MEW threads are aligned to the tensile direction of load, running predominantly along the longitudinal axis. As tensile load is applied to the scaffold, the threads can effectively carry the load. This is shown in

**ADVANCED
SCIENCE NEWS**

www.advancedsciencenews.com

**ADVANCED
ENGINEERING
MATERIALS**

www.aem-journal.com

Figure 4g, where little deformation is observed in the 21.8° scaffold during loading. However, as the pore angle increases, the threads are aligned more circumferentially, making them ineffective at resisting tensile load. When load is applied to these scaffolds, the fibers must first reorient, enabling them to better carry the tensile load. This results in a "Chinese finger trap" morphology, as shown in Figure 4h–i. The toe region of these scaffolds is associated with morphology change of the scaffolds, into a shape better suited to resisting tensile load.

Figure 4d–f shows a map of the initial stiffness, secondary stiffness, and transition point for both varying pore angle and area (or varying circumferential and longitudinal nodes). Studying the isolines of these further elucidates the mechanical behavior of these scaffolds. For example, in Figure 4f, isolines of constant transition point are highly correlated to the pore angle, suggesting an effective means of tailoring transition point. This matches the analysis in the previous paragraph on morphological realignment. Further, the secondary stiffness (Figure 4e) is predominantly controlled by the number of circumferential nodes (more circumferential nodes mean more threads). Finally, for low pore angle, the initial stiffness (Figure 4d) is predominantly controlled by pore angle; however, for larger pore angle, initial stiffness is predominantly controlled by circumferential nodes.

### 2.4.2. Compression

Similar to tensile loading, the compressive behavior varies dramatically with respect to pore area and angle (see **Figure 5**). Figure 5a shows the load–deformation behavior of three indicative scaffolds with different pore angles. Like tensile loading, the initial deformation of the scaffolds is linear. However, under compression the scaffolds are susceptible to buckling, which can occur in a gradual or spontaneous manner.

For example, the 21.8° scaffold, with threads aligned longitudinally, has the greatest compressive stiffness. However, because of this, the scaffold has limited capacity to deform leading to spontaneous buckling (Figure 5a, point II). In the FE model, buckling is exhibited by a reduction in the reaction force causing the FE model to fail to converge; as such, no data are collected postbuckling. Comparatively, the 95.4° scaffold has a lower compressive stiffness enabling it to exhibit large deformation.

Compressive stiffness of the scaffolds as a function of pore angle is shown in Figure 5b. Like tensile loading, compressive stiffness is highly dependent on pore angle, varying by a factor of 204× over the investigated range (from 2.91 to 594 N m$^{-1}$, with low pore angle scaffolds being significantly stiffer than their high pore angle counterparts.
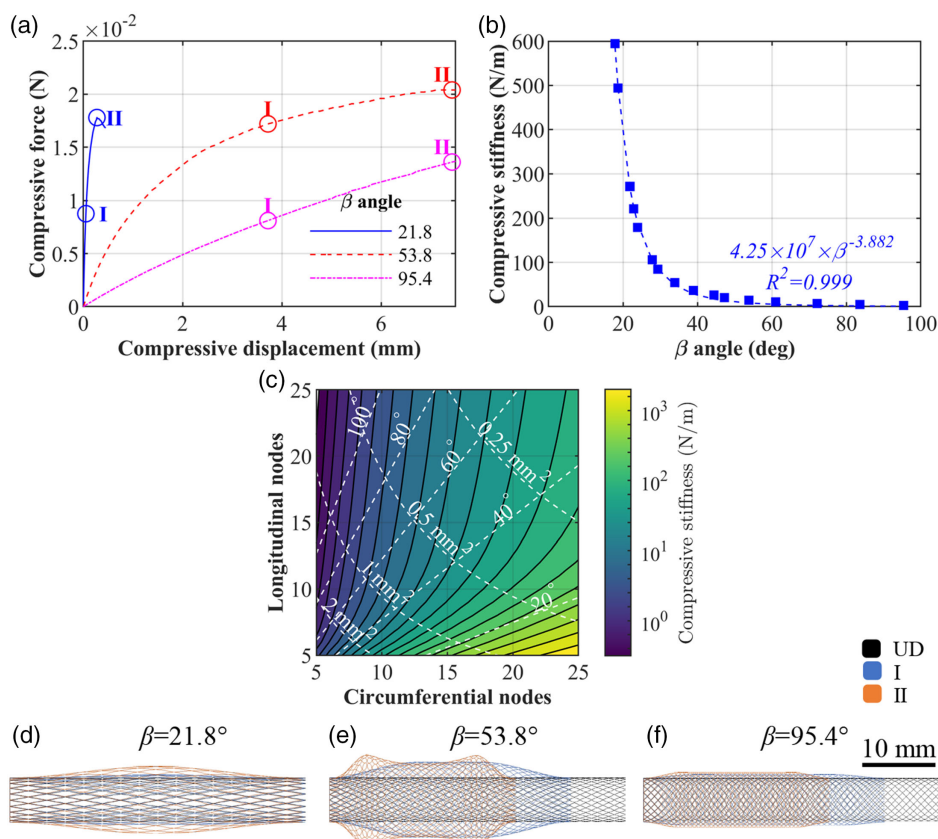


**Figure 5.** Compressive behavior of scaffolds predicted by FE model. a) Force–displacement curve of the indicative scaffolds, showing typical behavior. b) Compressive stiffness of the scaffolds as a function of pore angle. c) Color map of compressive initial stiffness as a function of pore angle and pore area (or circumferential and longitudinal nodes). d–f) Deformation behavior of the indicative scaffolds from (a) showing the scaffold morphology in their UD state, partially deformed state (I) and maximally deformed state (II).

**2200479 (5 of 11)**

**ADVANCED
SCIENCE NEWS**

www.advancedsciencenews.com

**ADVANCED
ENGINEERING
MATERIALS**

www.aem-journal.com

Finally, a map of compressive stiffness is shown in Figure 5e for varying pore angle and pore area (or number of longitudinal and circumferential nodes). As both compression and tension are forms of uniaxial loading, the stiffness behaviors of these are intrinsically linked and cannot be independently tuned. This is demonstrated in Figure 4d and 5c where the initial stiffness of the scaffolds under tension and compression shows strong alignment (this is further explored in Section 2.6).

### 2.4.3. Bending

The bending behavior of scaffolds as predicted by the FE model is shown in **Figure 6**. Figure 6a shows the load–deformation behavior of three indicative scaffolds with different pore angles. Like tension and compression, the initial behavior of the scaffolds under bending is linear. In fact, bending is a complex deformation in which one side of the scaffold experiences tension while the other experiences compression. As such, the low pore angle scaffolds are susceptible to buckling on their compressive side. This is apparent in the 21.8° which exhibited high stiffness under

bending but buckled at approximately 6° (Figure 6a, point II). In comparison, the 95.4° scaffold was able to rotate the full 90° while maintaining linear behavior and not exhibiting buckling. The 53.8° scaffold buckled at 86° of rotation.

The bending stiffness of the scaffolds as a function of pore angle is shown in Figure 6b, while Figure 6c shows a map of bending stiffness as a function of pore angle and pore area (or longitudinal and circumferential node numbers). As bending embodies both tensile and compressive loading, the trend for these plots is like that for tension and compression. Over the ranges investigated, for a constant pore area of 0.5 mm², the bending stiffness varied by a factor of 231× (from $6.18 \times 10^{-8}$ to $1.42 \times 10^{-5}$ Nm deg$^{-1}$).

### 2.4.4. Radial

Radial loading encompasses both radial expansion (tension) and compression, which for simplicity are shown together in **Figure 7**. Load–deformation curves of three indicative scaffolds are shown in Figure 7a. Unlike tension, compression, and
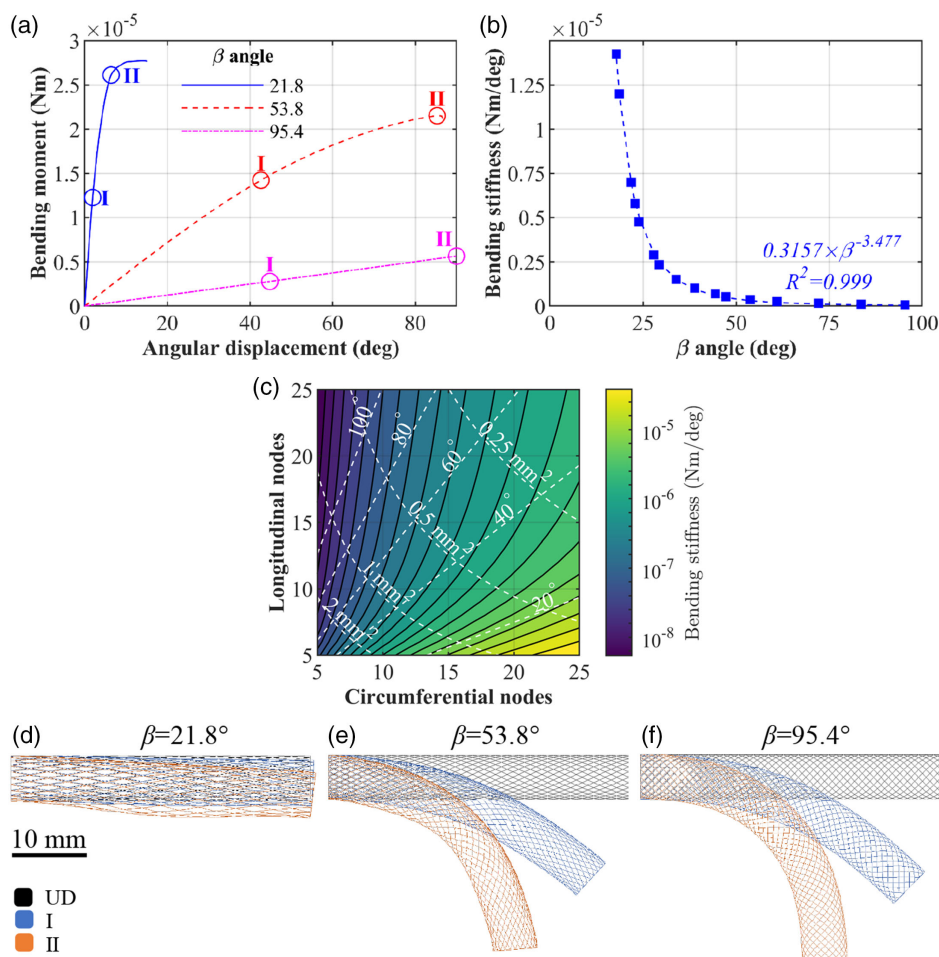


**Figure 6.** Bending behavior of scaffolds predicted by FE model. a) Moment-rotation curve of the indicative scaffolds, showing typical behavior. b) Bending stiffness of the scaffolds as a function of pore angle. c) Color map of bending initial stiffness as a function of pore angle and pore area (or circumferential and longitudinal nodes). d–f) Deformation behavior of the indicative scaffolds from (a) showing the scaffold morphology in their UD state, partially deformed state (I) and maximally deformed state (II).
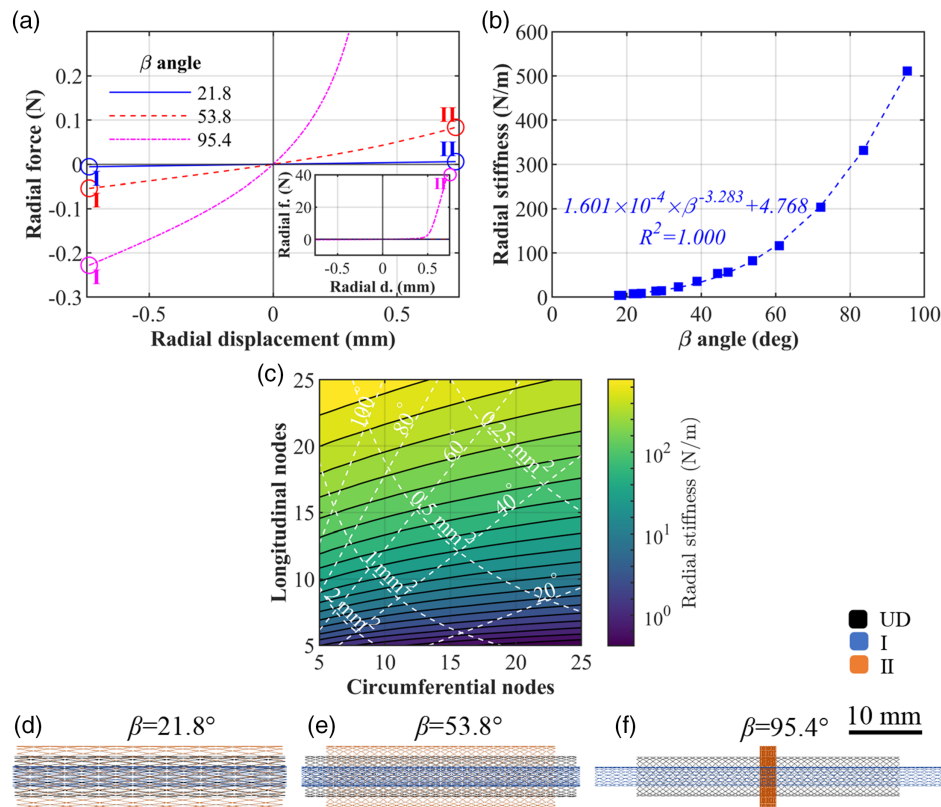
**Figure 7.** Radial tension and compression behavior of scaffolds predicted by FE model. a) Load–displacement curves of the indicative scaffolds, showing typical behavior. b) Radial stiffness of the scaffolds as a function of pore angle. c) Color map of radial initial stiffness as a function of pore angle and pore area (or circumferential and longitudinal nodes). d–f) Deformation behavior of the indicative scaffolds from (a) showing the scaffold morphology in their UD state, partially deformed state (I), and maximally deformed state (II).

bending, the stiffness nature of these scaffolds under radial loading is the opposite with the low pore angle scaffold being the softest and the high pore angle scaffold being the stiffest. This is further reflected in Figure 7b which shows the radial stiffness as a function of pore angle. Here, radial stiffness is positively correlated with pore angle, varying by a factor of 124× over the range investigated (4.12 to 511 N m$^{-1}$).

Due to the geometry of the scaffolds, under radial loading, the scaffolds experienced a change in their end-to-end length. Under radial tension, the individual threads align more circumferentially, shortening the scaffold length. While under radial compression, the threads align more longitudinally, increasing scaffold length. This length change is the most prominent for the 95.4° scaffold which exhibits large length change (Figure 7f). A special case is shown for this scaffold where at approximately 0.5 mm radial tension, fibers are almost completely circumferentially aligned, indicated by a scaffold of minimal length, and a dramatic increase in stiffness. Conversely, this length change is the least for the 21.8° scaffold, which offers the least resistance to radial loading (Figure 7d).

A full map of radial stiffness as a function of scaffold pore angle and pore area (or number of longitudinal and circumferential nodes) is shown in Figure 7c. Over this range of investigated parameters, stiffness varies by a factor of 2690×

(from 0.425 to 1140 N m$^{-1}$). For radial stiffness, this is most influenced by the number of longitudinal nodes.

### 2.5. Independence of Loading Stiffness

The nature of tension, compression, and bending loading is similar, as each involves axial loading of the scaffold. In the case of bending, one side of the scaffold experiences axial tension, while the other experiences axial compression. This similar nature intrinsically links the stiffness of the scaffold under these loading regimes. Conversely, radial loading is unique, as it does not involve an axial component.

As tension, compression, and bending stiffness are intrinsically linked, they cannot be independently tuned. This is shown in **Figure 8**a,b, which shows a linear relationship between the initial tensile stiffness and that of compression and bending. Conversely, radial stiffness can be tuned independently of tensile stiffness, as shown in Figure 8c.

### 3. Discussion

Tissue engineered structures must exhibit favorable mechanical behaviors specific to their applications. To this end, research has largely focused on employing biomimetic design strategies with
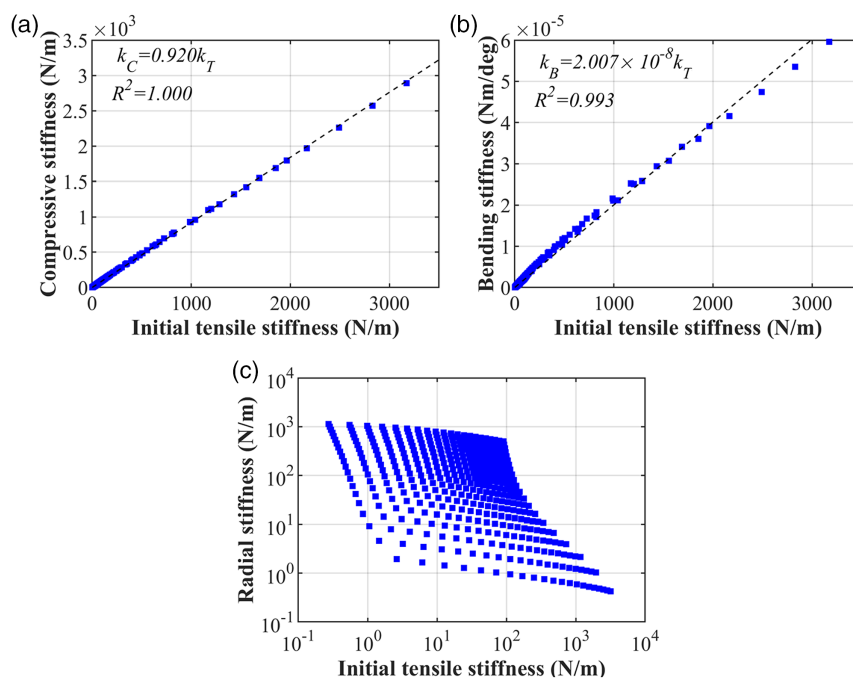
**Figure 8.** Comparison of tensile stiffness to the a) compressive stiffness, b) bending stiffness, and c) radial stiffness of the 421 simulated scaffolds. For tensile stiffness, only the initial tensile stiffness is considered.

the aim of replicating the mechanical properties of native tissues.[38,39] Factors such a strut or fiber size, pore size or fiber spacing, and pattern are routinely tuned to achieve specific mechanical responses to match that of native tissues.[40,41] Compared to traditional manufacturing techniques, 3D printing adds the capacity to tune the geometric structure of a scaffold, adding unparalleled capacity to tailor mechanical behavior. However, the ability to tune the mechanical properties of tubular MEW scaffolds remains in its infancy, and papers which demonstrate tunability only do so over a small range.[13] In comparison, in this study we demonstrate massive tunability to the factor of 294× for tension, 204× for compression, 231× for bending, and 124× for radial loading.

The bilinear, "j-shaped," force–deformation curve is commonly found in biological tissue such as ligaments and tendons,[42–44] vascular tissues,[45] and is observed in collagen at the molecular scale.[46] For this reason, tissue engineered structures have sought to replicate this behavior.[23,45,47] Our work leapfrogs current research efforts by not only demonstrating that the "j-shape" curve is readily achieved with MEW crosshatch scaffolds but also exploring in detail how geometric parameters can be selected to effectively tune the individual stages of the curve. Through large-scale simulation of 421 different scaffold geometries, we have shown that the transition point is predominantly controlled by the scaffold pore angle, while the pore angle and pore area can be tuned to select the stiffness of each region.

Furthermore, this model provides an automated method for predicting the bending deformation behavior of tubular MEW scaffolds previously not achieved in the literature. The results from this model provide both predictions of stress–strain behavior, consistent with previously published experimental studies

investigating the bending behavior of MEW tubes,[12,18] in addition to visualization of the bending deformation and its influence on unit cell geometry.

This work also highlights some limitations of the crosshatch scaffold design. It is demonstrated that tension, compression, and bending stiffness of these scaffolds are inherently coupled, such that the impact of pore angle and pore area control the stiffness of these in a similar way. This is because all three of these loading modes involve uniaxial loading, with bending being a special case where one side of the scaffold is in tension, while the other is in compression. In areas where these stiffnesses must be independently controlled, the crosshatch design is limited. For example, in trachea tissue engineering, to mimic the properties of native tissue, scaffolds must be longitudinally stiff while allowing flexibility under bending.[48] This cannot be effectively achieved with a crosshatch design, motivating the exploration of alternative tubular MEW designs.

Efforts to optimize the mechanical response of scaffolds must also consider how these factors simultaneously impact the biological response of seeded cells during in vitro studies and tissue ingrowth when implanted in in vivo models. Research has shown the influence of pore geometry and fiber size on the growth and proliferation of cells.[23,25,49] Specific scaffold design elements such as porosity, bending stiffness, and pore size are often competing requirements to achieve both the desired mechanical and biological properties. Requiring extensive experimental iterations, design flexibility for optimized scaffolds for specific tissue engineering contexts is limited and has motivated the use of models to predict and optimize scaffold designs. In this space, our work provides design guidance by unravelling how crosshatch pore geometry controls the mechanical behavior.

Despite the known complex relationship between scaffold design and tissue engineering functionality, crosshatch scaffolds have been the preferred geometry for MEW tubular scaffolds due to the ease of programming the required gcode using a continuous path.[7] "Written" crosshatch tubular scaffolds, as opposed to meshes with aligned but nonstacked fibers,[21,50,51] require the ability to program the ratio of mandrel rotation and transverse travel speed to "stack" fibers on top of one another to create defined crosshatch pores, as initially reported by McColl et al.[18] However, these can still be readily fabricated using a constantly rotating mandrel. While more complex designs are achievable using a flat collector plate,[1] only recently MEW machines have been upgraded to enable more complex tubular scaffold designs using nonlinear rotation paths.[9,22] In this study, tubular scaffolds with crosshatch architecture were therefore investigated, using this well-studied geometry to explore the ability to predict microfiber tubular scaffold mechanical behavior using an FE model. The expansion of the model presented in this study to enable the prediction of mechanical deformation of scaffolds with more complex architectures is an exciting avenue for further research.

The model presented here was designed for elastic deformation, incorporated linear-elastic material properties, and was successfully validated for these conditions. While the model does exhibit buckling behavior, the model was not validated for this due to the complexity of buckling and because buckling is outside of the desired operation of tissue scaffolds. The FE model was based upon an idealized version of the MEW scaffold. This includes idealizing the thread cross section as rectangular (see Supporting Information, Section 1) and idealizing the complex thread junctions (see Figure 2b). These idealizations are considered valid, demonstrated by successful model validation. However, the complex geometry of the junction present in MEW scaffolds raises this as an important area of investigation in future research. In particular, the bond-separation effect at junctions would be a valuable area of future research to understand how this effects mechanics and failure.

## 4. Conclusion

MEW is a promising emerging technology for engineering tubular tissue scaffolds. The design and optimization of these scaffolds seek to mimic the mechanical behavior of native tissue while considering pore geometry which impacts cell attachment and proliferation. This work is the first to undergo a detailed assessment of the impact of pore geometry on the mechanical behavior of crosshatch MEW scaffolds. Through simulating 421 different crosshatch geometries, under multiple loading environments, the massive tailorability of these scaffolds was demonstrated. Over the parameters explored in this study, scaffold stiffness could be modified by 294× for tension, 204× for compression, 231× for bending, and 124× for radial loading. The stiffness relations presented in this work act as a valuable design tool for crosshatch MEW scaffolds.

## 5. Experimental Section

*Thread and Scaffold Fabrication*: MEW samples were fabricated using a custom-built MEW device, described previously.[7] Prior to fabrication, PCL (CAPA 6430, Perstorp) was heated at 90 °C for 20 min in a 3 mL syringe (Nordson EFD) fitted with a grounded 21 G needle (Nordson EFD). Extrusion was performed under constant 0.05 MPa air pressure, with 5 mm tip-to-collector distance, and 5.8 kV applied to a collector plate.

To measure the elastic modulus of MEW PCL threads, 12 threads were manufactured on a flat collector plate, 120 mm in length, and consisting of ten fibers.

To validate the FE model, crosshatch tubular scaffolds were fabricated by printing onto a 16 mm diameter rotating mandrel using gcode generated using a previously published scaffold design tool.[7] The scaffolds were fabricated with a targeted pore area of 0.5 mm$^2$ and targeted pore angles of 20°, 50°, and 90°. The pore size and angles were then automatically adjusted to accommodate for the integer number of circumferential and longitudinal junctions, resulting in scaffolds with angles of 21.8°, 53.8°, and 95.4°, respectively. All scaffolds were approximately 40 mm in length, ten fiber layers high, and were printed in replicate for tensile testing and imaging.

*Thread and Scaffold Mechanical Testing*: To determine the elastic modulus of individually fabricated MEW PCL threads, uniaxial tensile testing was conducted on the individually fabricated threads and the elastic modulus was calculated from the linear section of the stress–strain curve. To determine the load–deformation behavior of the fabricated MEW scaffolds, uniaxial tensile testing was conducted on the fabricated scaffolds. For this, the threads and scaffolds were mounted in a uniaxial tensile testing machine (Tytron 250 Microforce Testing System, 250 N load cell, calibrated at ±25 and ±2.5 N with 2.5 mN resolution). Threads were loaded to failure at a rate of 50 mm min$^{-1}$ while scaffolds were loaded at 1.1% strain s$^{-1}$.

*SEM Imaging of Threads and Scaffolds*: PCL threads and scaffolds were imaged using SEM (MIRA3, Tescan, Czechia). Samples were initially sputter coated with gold for 5 min to achieve ≈20 nm gold coating. Imaging was performed using 8.0 beam intensity and 3.0 kV voltage at 100× and 500× magnification. Fiber diameter was measured using the ImageJ measurement tool in replicates ($n = 10$).

*FE Model*: A FE model of the scaffolds was created in Ansys v20.1. In the model, based upon beam elements, each strut of the scaffold was meshed by five BEAM189 elements and mesh convergence was confirmed. The cross section of each thread was idealized as a rectangle with dimensions of 22 × 220 μm. This was based upon SEM measurement of the MEW threads (see Section 2.3). The MEW PCL was assumed to behave in a linear-elastic manner with an elastic modulus of 450 MPa (see Section 2.3). The model was solved under large deformation conditions.

For uniaxial tension/compression and bending, a node was located at the center of the base (referred to as the support node). Nodes at the scaffold's base were rigidly bonded to the support node using rigid beam elements (MPC184) and the support node was fixed in all degrees of freedom. Likewise, a node was located at the center of the free end (referred to as the load node). Nodes at the scaffold's free end were rigidly bonded to the load node using rigid beam elements (MPC184).

Loading in the FE model was performed under displacement control. For uniaxial tension/compression, axial displacement was applied directly to the load node, which was fixed from movement in the transverse directions. For bending load, a bending rotation was applied to the load node, which was fixed from movement outside the plane of bending. The resulting reactions were measured at both the support node and load node.

For radial tension/compression, nodes of the scaffold base were fixed from movement in the axial direction. For loading, a radial displacement was applied to the nodes of each junction. Likewise, the reaction at each junction was measured and summated to determine the total radial force.

*FE Study Design*: The FE component was separated into three studies. The first study focused on validating the FE model. For this, FE models were created of the fabricated MEW scaffolds and loaded in 100 load steps to 2, 4, and 14 mm, respectively, for the 21.8°, 53.8°, and 95.4° scaffolds.

In the second study, the impact of varying pore angle, while maintaining a constant pore area of 0.5 mm$^2$, was investigated. Scaffold geometries were created with pore angles of between 17.8° and 95.4°. As pore area is a function of the radial and longitudinal junction number, it is often not possible to create scaffolds with a pore area of exactly 0.5 mm$^2$; the true pore

areas in this study varied between 0.476 and 0.524 mm². Table S2, Supporting Information, lists the scaffold geometries investigated.

In the third study, the impact of varying both pore angle and pore area was investigated. In this, all permutations, with circumferential and radial junctions between 5 and 25, were investigated. Scaffolds simulated in the second and third FE study were 20 mm in length and 3 mm in diameter; this was chosen to better replicate the geometry of vascular stents.[37]

## Supporting Information

Supporting Information is available from the Wiley Online Library or from the author.

## Conflict of Interest

The authors declare no conflict of interest.

## Data Availability Statement

The data that support the findings of this study are available from the corresponding author upon reasonable request.

[1] T. M. Robinson, D. W. Hutmacher, P. D. Dalton, *Adv. Funct. Mater.* **2019**, *29*, 1904664.

[2] N. C. Paxton, R. Lamont, T. L. Brooks-Richards, M. A. Woodruff, *J. 3D Print. Med.* **2021**, *5*, 10.

[3] M. Lanaro, L. Booth, S. K. Powell, M. A. Woodruff, in *Electrofluidodynamic Technologies (EFDTs) for Biomaterials and Medical Devices: Principles and Advances*, Woodhead Publishing, Cambridge, MA, USA **2018**, pp. 37–69.

[4] N. C. Paxton, J. Ren, M. J. Ainsworth, A. K. Solanki, J. R. Jones, M. C. Allenby, M. M. Stevens, M. A. Woodruff, *Macromol. Rapid Commun.* **2019**, *40*, 1900019.

[5] J. C. Kade, P. D. Dalton, *Adv. Healthcare Mater.* **2021**, *10*, 2001232.

[6] P. D. Dalton, *Curr. Opin. Biomed. Eng.* **2017**, *2*, 49.

[7] N. C. Paxton, M. Lanaro, A. Bo, N. Crooks, M. T. Ross, N. Green, K. Tetsworth, M. C. Allenby, Y. Gu, C. S. Wong, S. K. Powell, M. A. Woodruff, *J. Mech. Behav. Biomed. Mater.* **2020**, *105*, 103695.

[8] K. A. van Kampen, E. Olaret, I.-C. Stancu, L. Moroni, C. Mota, *Mater. Sci. Eng., C* **2021**, *119*, 111472.

[9] K. Somszor, O. Bas, F. Karimi, T. Shabab, N. T. Saidy, A. J. O'Connor, A. V. Ellis, D. W. Hutmacher, D. E. Heath, *ACS Macro Lett.* **2020**, *9*, 1732.

[10] A. Ravichandran, C. Meinert, O. Bas, D. W. Hutmacher, N. Bock, *Mater. Sci. Eng., C* **2021**, *128*, 112313.

[11] P. Mieszczanek, T. M. Robinson, P. D. Dalton, D. W. Hutmacher, *Adv. Mater.* **2021**, *33*, 2100519.

[12] A. M. van Genderen, K. Jansen, M. Kristen, J. van Duijn, Y. Li, C. C. L. Schuurmans, J. Malda, T. Vermonden, J. Jansen, R. Masereeuw, M. Castilho, *Front. Bioeng. Biotechnol.* **2021**, *8*, 617364.

[13] N. T. Saidy, A. Fernández-Colino, B. Shiroud Heidari, R. Kent, M. Vernon, O. Bas, S. Mulderrig, A. Lubig, J. C. Rodríguez-Cabello, B. Doyle, D. W. Hutmacher, E. M. De-Juan-Pardo, P. Mela, *Adv. Funct. Mater.* **2022**, *32*, 2110716.

[14] T. L. Brooks-Richards, N. C. Paxton, M. C. Allenby, M. A. Woodruff, *Mater. Des.* **2022**, *215*, 110466.

[15] N. Pien, M. Bartolf-Kopp, L. Parmentier, J. Delaey, L. De Vos, D. Mantovani, S. Van Vlierberghe, P. Dubruel, T. Jungst, *Macromol. Mater. Eng.* **2022**, *307*, 2200097.

[16] T. D. Brown, A. Slotosch, L. Thibaudeau, A. Taubenberger, D. Loessner, C. Vaquette, P. D. Dalton, D. W. Hutmacher, *Biointerphases* **2012**, *7*, 1.

[17] T. Jungst, M. L. L. Muerza-Cascante, T. D. Brown, M. Standfest, D. W. Hutmacher, J. Groll, P. D. Dalton, *Polym. Int.* **2015**, *64*, 1086.

[18] E. McColl, J. Groll, T. Jungst, P. D. P. D. Dalton, *Mater. Des.* **2018**, *155*, 46.

[19] T. Jungst, I. Pennings, M. Schmitz, A. J. W. P. Rosenberg, J. Groll, D. Gawlitta, *Adv. Funct. Mater.* **2019**, *29*, 1905987.

[20] E. C. L. Bolle, N. Bartnikowski, P. Haridas, T. J. Parker, J. F. Fraser, S. D. Gregory, T. R. Dargaville, *J. Biomed. Mater. Res. Part B* **2020**, *108*, 738.

[21] N. T. Saidy, T. Shabab, O. Bas, D. M. Rojas-González, M. Menne, T. Henry, D. W. Hutmacher, P. Mela, E. M. De-Juan-Pardo, *Front. Bioeng. Biotechnol.* **2020**, *8*, 793.

[22] N. C. Paxton, R. Daley, D. P. Forrestal, M. C. Allenby, M. A. Woodruff, *Mater. Des.* **2020**, *193*, 108787.

[23] N. T. Saidy, F. Wolf, O. Bas, H. Keijdener, D. W. Hutmacher, P. Mela, E. M. De-Juan-Pardo, *Small* **2019**, *15*, 1900873.

[24] F. Tourlomousis, C. Jia, T. Karydis, A. Mershin, H. Wang, D. M. Kalyon, R. C. Chang, *Microsyst. Nanoeng.* **2019**, *5*, 15.

[25] P. R. Buenzli, M. Lanaro, C. S. Wong, M. P. McLaughlin, M. C. Allenby, M. A. Woodruff, M. J. Simpson, *Acta Biomater.* **2020**, *114*, 285.

[26] C. Xie, Q. Gao, P. Wang, L. Shao, H. Yuan, J. Fu, W. Chen, Y. He, *Mater. Des.* **2019**, *181*, 108092.

[27] I. Pennings, E. Van Haaften, T. Jungst, J. A. Bulsink, A. J. W. P. Rosenberg, J. Groll, C. V. Bouten, N. A. Kurniawan, A. I. P. M. Smits, D. Gawlitta, *Biofabrication* **2019**, *12*, 015009.

[28] A. B. McCosker, M. E. Snowdon, R. Lamont, M. A. Woodruff, N. C. Paxton, *Adv. Mater. Technol.* **2022**, 2200259, https://doi.org/10.1002/admt.202200259.

[29] F. M. Wunner, O. Bas, N. T. Saidy, P. D. Dalton, D. W. Hutmacher, E. M. D.-J. Pardo, *J. Visualized Exp.* **2017**, *2017*, e56289.

[30] B. D. Riehl, J. H. Park, I. K. Kwon, J. Y. Lim, *Tissue Eng., Part B* **2012**, *18*, 288.

[31] J. C. Kade, P. F. Otto, R. Luxenhofer, P. D. Dalton, *Polym. Adv. Technol.* **2021**, *32*, 4951.

[32] J.-M. Chen, J. Lee, J.-W. Yang, S.-H. Lin, Y.-T. Lin, S.-J. Liu, *Appl. Sci.* **2020**, *10*, 3189.

**ADVANCED
SCIENCE NEWS**

www.advancedsciencenews.com

**ADVANCED
ENGINEERING
MATERIALS**

www.aem-journal.com

[33] J.-Z. Liang, D.-R. Duan, C.-Y. Tang, C.-P. Tsui, D.-Z. Chen, S.-D. Zhang, *J. Polym. Eng.* **2014**, *34*, 69.

[34] H.-C. Dang, W.-C. Nie, X.-L. Wang, W.-T. Wang, F. Song, Y.-Z. Wang, *RSC Adv.* **2014**, *4*, 53380.

[35] A. Khalilimeybodi, A. Alishzadeh Khoei, B. Sharif-Kashani, *Cardiovasc. Eng. Technol.* **2020**, *11*, 188.

[36] Q. Zheng, P. Dong, Z. Li, X. Han, C. Zhou, M. An, L. Gu, *Nanotechnol. Rev.* **2019**, *8*, 168.

[37] J. Butany, K. Carmichael, S. W. Leong, M. J. Collins, *J. Clin. Pathol.* **2005**, *58*, 795.

[38] H. D. Kim, S. Amirthalingam, S. L. Kim, S. S. Lee, J. Rangasamy, N. S. Hwang, *Adv. Healthcare Mater.* **2017**, *6*, 1700612.

[39] P. Datta, V. Vyas, S. Dhara, A. R. Chowdhury, A. Barui, *J. Bionic Eng.* **2019**, *16*, 842.

[40] D. Olvera, M. Sohrabi Molina, G. Hendy, M. G. M. G. Monaghan, D. Olvera, M. Sohrabi Molina, M. G. M. G. Monaghan, G. Hendy, *Adv. Funct. Mater.* **2020**, *30*, 1909880.

[41] M. Castilho, A. van Mil, M. Maher, C. H. G. Metz, G. Hochleitner, J. Groll, P. A. Doevendans, K. Ito, J. P. G. Sluijter, J. Malda, *Adv. Funct. Mater.* **2018**, *28*, 1803151.

[42] A. Sensini, L. Cristofolini, *Materials* **2018**, *11*, 1.

[43] J. H. C. Wang, *J. Biomech.* **2006**, *39*, 1563.

[44] G. Hochleitner, F. Chen, C. Blum, P. D. P. D. Dalton, B. Amsden, J. Groll, *Acta Biomater.* **2018**, *72*, 110.

[45] H. S. Rapoport, J. Fish, J. Basu, J. Campbell, C. Genheimer, R. Payne, D. Jain, *Tissue Eng., Part C* **2012**, *18*, 567.

[46] M. Tang, T. Li, E. Pickering, N. S. Gandhi, K. Burrage, Y. T. Gu, *J. Mech. Behav. Biomed. Mater.* **2018**, *86*, 359.

[47] D. Zhalmuratova, T. G. La, K. T. T. Yu, A. R. A. Szojka, S. H. J. Andrews, A. B. Adesida, C. Il Kim, D. S. Nobes, D. H. Freed, H. J. Chung, *ACS Appl. Mater. Interfaces* **2019**, *11*, 33323.

[48] A. J. Boys, S. L. Barron, D. Tilev, R. M. Owens, *Front. Bioeng. Biotechnol.* **2020**, *8*, 1.

[49] F. Tourlomousis, W. Boettcher, H. Ding, R. C. Chang, *J. Micro Nano-Manuf.* **2017**, *4*, 1.

[50] A. Berner, J. Henkel, M. A. Woodruff, R. Steck, M. Nerlich, M. A. Schuetz, D. W. Hutmacher, *Stem Cells Transl. Med.* **2015**, *4*, 503.

[51] A. Berner, J. D. Boerckel, S. Saifzadeh, R. Steck, J. Ren, C. Vaquette, J. Q. Zhang, M. Nerlich, R. E. Guldberg, D. W. Hutmacher, M. A. Woodruff, *Cell Tissue Res.* **2012**, *347*, 603.